Journal of Luminescence 209 (2019) 109–115

Contents lists available at ScienceDirect

Journal of Luminescence

journal homepage: www.elsevier.com/locate/jlumin

# Multi-wavelength phosphor model based on fluorescent radiative transfer equation considering re-absorption effect

Yupu Ma, Jie Sun, Xiaobing Luo*

*School of Energy and Power Engineering, Huazhong University of Science and Technology, China*

ARTICLE INFO

*Keywords:*
Radiative transfer
Fluorescence
Phosphor modeling
Light-emitting diodes
Scattering

ABSTRACT

The light propagation properties within the phosphor layer in phosphor-converted light-emitting diodes (pc-LEDs) have been extensively described by the two-wavelength model, in which two individual excitation and emission wavelengths are selected. The ignorance of the wavelength-dependence may cause deviation and cannot return the spectrum. In this paper, we extended the two-wavelength model to a multi-wavelength model based on fluorescent radiative transfer equation (FRTE) to characterize the overall light propagation behavior in the phosphor layer. In addition to the light absorption, forward scattering, and fluorescence characteristics, the re-absorption effect was further considered. The spectral radiance at any spatial location and angular direction for each wavelength was iteratively solved using the spectral element method (SEM). The model was validated by comparing the calculated spectrum and angular correlated color temperature (CCT) with experiments and good agreement was achieved with the corresponding maximum deviations of 7.6% and 3.6%, respectively. We also conducted a comparison between the multi-wavelength model with the two-wavelength model. We found that the two-wavelength model may underestimate or overestimate the optical power in the blue region and yellow region, respectively. It was attributed to assuming the peak absorption coefficient and quantum efficiency for all excitation wavelengths in the two-wavelength model.

## 1. Introduction

Light propagating within the phosphor layer exhibits absorption, strong forward scattering, and fluorescence characteristics [1–4]. Numerical and analytical methods have been already proposed to model the phosphor in the last decade. Monto-Carlo ray-tracing simulation has been a very accurate numerical method in modeling the optical-related objects, making it the most widely applied method for phosphor modeling [5–7]. However, due to the probability-based computing method, usually a million rays or even more need to be traced to obtain accurate results [8]. To get a deep understanding of the light propagation properties inside the phosphor, researchers have proposed some analytical methods, including the diffusion-approximation (DA) method [9] and the extended Kubelka–Munk (KM) theory for fluorescence [2,10–12]. These methods have been demonstrated to be very efficient compared to the Monto-Carlo method. Recently, we have developed a general one-dimensional phosphor model based on the fluorescent radiative transfer equation (FRTE) [13], which is the governing equation to describe the overall light propagating properties of the fluorescent media. By calculating the radiance at any location and direction, we can evaluate the spatial and angular optical properties efficiently.

However, most of the mentioned methods are based on the two-wavelength method [5–7,9–12]. In other words, only peak excitation and emission wavelengths are selected to be solved. Typically for the cerium-doped yttrium aluminum garnet (YAG: Ce) phosphor excited by a blue light-emitting diode (LED), the individual blue and yellow lights are solved. In this case, the spectrum of the phosphor-converted lighting emitting diode (pc-LED) cannot be obtained. In addition, the ignorance of the wavelength-dependence of the phosphor parameters may also cause deviation of the calculated results. To solve this problem, many studies have further considered the wavelength-dependence using the Monto-Carlo simulation [14–16]. By inputting the excitation and emission spectrum and the wavelength-dependent phosphor parameters, the spectrum can be estimated accurately.

Alternatively, Leyre et al. have developed an analytical extended adding-doubling method considering the wavelength-dependence [17]. This method is demonstrated to be very efficient to predict the angular and spectral distribution of the fluorescent media. In their model, the excitation and emission spectrum does not overlap with each other. However, for most commercial phosphor materials, there is an overlap between the excitation and emission spectrum [1]. In this case, some of the converted light will be absorbed again by the phosphor particle and

* Corresponding author.
*E-mail address:* luoxb@hust.edu.cn (X. Luo).

https://doi.org/10.1016/j.jlumin.2019.01.038
Received 22 October 2018; Received in revised form 3 January 2019; Accepted 23 January 2019
Available online 24 January 2019

re-emitted as light with the longer wavelength, which is known as the re-absorption effect [18]. For phosphor with large spectral overlap, the re-absorption effect cannot be neglected. To include the re-absorption effect, Leyre et al. have also extended the analytical adding-doubling method to take the spectral overlap into account [19].

In this work, we extended the previous two-wavelength model to a multi-wavelength model based on FRTE considering the re-absorption effect. The wavelength domain was divided into many discrete wavelength nodes. For each wavelength, the FRTE and the boundary conditions were established. Then, this series of complicated partial differential-integral equations (FRTEs) was solved using the spectral element method (SEM) [20], which has been successfully applied to solve RTE [21], and two-wavelength FRTEs [13]. The spectral radiance at any spatial location and angular direction for each wavelength was calculated by using this method. Next, the output spectral radiant flux distribution and then the optical power, luminous flux, average correlated color temperature (CCT) and color rendering index (CRI) were calculated. In addition, the angular CCT and spectral radiant intensity distribution were also obtained. In the following, the model was validated by comparing these calculated properties with experiments. Finally, the presented multi-wavelength model was compared with the two-wavelength model.

## 2. Model definition

Fig. 1 illustrates the schematic of the one-dimensional phosphor model and the boundary conditions. For a planar phosphor plate with a large ratio of the diameter to the thickness, the one-dimensional assumption can be feasible, i.e., the optical variables only vary along the thickness (z-) direction [13]. We can see that in the middle filled area, when excitation light (usually blue light) hits the phosphor particle, part of the light is absorbed and the other is scattered without being absorbed. Some of the absorbed light is then down-converted to green-yellow light by the Stokes shift. The converted light may be re-absorbed by the neighboring phosphor particles and then again down-converted to light with a longer wavelength. This is also called the re-absorbing effect, which may pose an effect on the optical performance of phosphor. In the following, the method of evaluating the re-absorption effect, as well as the mentioned light propagating properties, will be presented.

Fig. 2 shows the excitation and emission spectrum (the normalized intensity are respectively denoted as $f_{ex}$ and $f_{em}$) of a typical YAG:Ce phosphor applied in pc-LEDs. There is a large spectral overlap between them, which ranges from $\lambda_{c,1}$ ($f_{em}=0$) to $\lambda_{c,2}$ ($f_{ex}=0$). These two critical values divide the full visible spectrum ranging from 380 nm to 780 nm into three regions, i.e., the excitation region ($\lambda_{ex}$), the

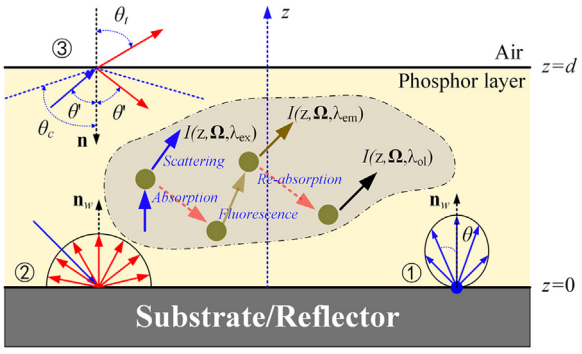


**Fig. 1.** Schematic of the one-dimensional phosphor model and boundary conditions. Conditions 1, 2 and 3 denote the incident LED Lambertian intensity, diffuse reflection at the substrate/reflector surface, and the Fresnel reflection at the phosphor-air interface, respectively. The middle filled area describes the schematic of the light propagation properties within the phosphor layer, including absorption, scattering, fluorescence, and re-absorption.

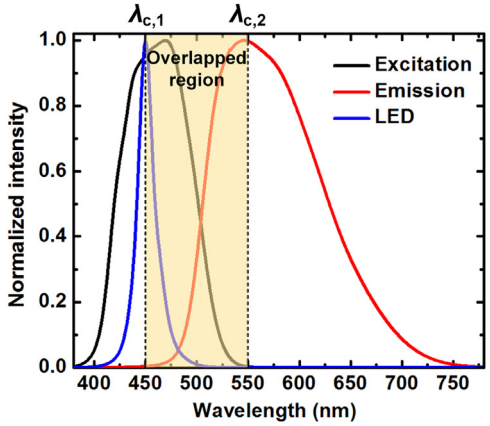


**Fig. 2.** The excitation and emission spectrum of YAG: Ce phosphor, and the emission spectrum of the blue LED used in this study. The yellow filled area (ranging from $\lambda_{c,1}$ to $\lambda_{c,2}$) denotes the spectrum overlapped region between the excitation and emission spectrum.

overlapped region ($\lambda_{ol}$), and the emission region ($\lambda_{em}$), corresponding to the marked three types of spectral radiance $I(z, \mathbf{\Omega}, \lambda_{ex})$, $I(z, \mathbf{\Omega}, \lambda_{ol})$, and $I(z, \mathbf{\Omega}, \lambda_{em})$ to be solved in Fig. 1. Then, these three regions are uniformly discretized into $N_{ex}$, $N_{ol}$, and $N_{em}$ wavelength nodes with the corresponding interval of $\Delta\lambda_{ex}$, $\Delta\lambda_{ol}$, and $\Delta\lambda_{em}$, respectively. According to the previous literatures [13,22], a series of extended governing FRTEs in one dimension for the excitation, overlapped, and emission regions can be respectively expressed as (1)-(3).

For each wavelength $\lambda_{ex,i}$ ($i = 1,2,\ldots,N_{ex}$) in the excitation region, only light absorption and scattering occur:

$$\mu\frac{dI(z,\mathbf{\Omega},\lambda_{ex,i})}{dz} = -[\kappa_a(\lambda_{ex,i}) + \kappa_s(\lambda_{ex,i})]\cdot I(z,\mathbf{\Omega},\lambda_{ex,i}) + \frac{\kappa_s(\lambda_{ex,i})}{4\pi}\int_{4\pi} I(z,\mathbf{\Omega},\lambda_{ex,i})p(\mathbf{\Omega},\mathbf{\Omega}')d\mathbf{\Omega}' \quad (1)$$

For each wavelength $\lambda_{ol,k}$ ($k = 1,2,\ldots,N_{ol}$) in the overlapped region, besides light absorption and scattering, the fluorescence and re-absorption occur simultaneously:

$$\begin{aligned}\mu\frac{dI(z,\mathbf{\Omega},\lambda_{ol,k})}{dz} &= -[\kappa_a(\lambda_{ol,k}) + \kappa_s(\lambda_{ol,k})]\cdot I(z,\mathbf{\Omega},\lambda_{ol,k}) \\ &+ \frac{\kappa_s(\lambda_{ol,k})}{4\pi}\int_{4\pi} I(z,\mathbf{\Omega},\lambda_{ol,k})p(\mathbf{\Omega},\mathbf{\Omega}')d\mathbf{\Omega}' \\ &+ \frac{1}{4\pi}\sum_{i=1}^{N_{ex}}\left\{\kappa_a(\lambda_{ex,i})\eta_{QE}(\lambda_{ex,i})\eta_{SS}(\lambda_{ex,i})\right. \\ &\left.\omega(\lambda_{ex,i},\lambda_{ol,k})\left[\int_{4\pi} I(z,\mathbf{\Omega},\lambda_{ex,i})d\mathbf{\Omega}\right]\triangle\lambda_{ex}\right\} \\ &+ \frac{1}{4\pi}\sum_{j=1}^{k-1}\left\{\kappa_a(\lambda_{ol,j})\eta_{QE}(\lambda_{ol,j})\eta_{SS}(\lambda_{ol,j})\right. \\ &\left.\omega(\lambda_{ol,j},\lambda_{ol,k})\left[\int_{4\pi} I(z,\mathbf{\Omega},\lambda_{r,j})d\mathbf{\Omega}\right]\triangle\lambda_{ol}\right\}\end{aligned} \quad (2)$$

For each wavelength $\lambda_{em,j}$ ($j = 1,2,\ldots,N_{em}$) in the emission region, there is no re-absorption. And light absorption, scattering, and fluorescence occur simultaneously:

$$\mu\frac{dI(z,\boldsymbol{\Omega},\lambda_{em,j})}{dz} = -[\kappa_a(\lambda_{em,j})+\kappa_s(\lambda_{em,j})]\cdot I(z,\boldsymbol{\Omega},\lambda_{em,j}) + \frac{\kappa_s(\lambda_{em,j})}{4\pi}\int_{4\pi} I(z,\boldsymbol{\Omega},\lambda_{em,j})p(\boldsymbol{\Omega},\boldsymbol{\Omega}')d\boldsymbol{\Omega}' + \frac{1}{4\pi}\sum_{i=1}^{N_{ex}}\left\{\kappa_a(\lambda_{ex,i})\eta_{QE}(\lambda_{ex,i})\eta_{SS}(\lambda_{ex,i})\right. \left.\omega(\lambda_{ex,i},\lambda_{em,j})\left[\int_{4\pi} I(z,\boldsymbol{\Omega},\lambda_{ex,i})d\boldsymbol{\Omega}\right]\triangle\lambda_{ex}\right\} + \frac{1}{4\pi}\sum_{k=1}^{N_{ol}}\left\{\kappa_a(\lambda_{ol,k})\eta_{QE}(\lambda_{ol,k})\eta_{SS}(\lambda_{ol,k})\right. \left.\omega(\lambda_{ol,k},\lambda_{em,j})\left[\int_{4\pi} I(z,\boldsymbol{\Omega},\lambda_{ol,k})d\boldsymbol{\Omega}\right]\triangle\lambda_{ol}\right\} \quad (3)$$

where $I(z, \boldsymbol{\Omega}, \lambda)$ denotes the spectral radiance at spatial location z and angular direction $\boldsymbol{\Omega}$ for the selected wavelength λ; $\mu$ is the direction cosine along z-direction; $\kappa_a$ and $\kappa_s$ are the absorption and scattering coefficients, respectively; $p(\boldsymbol{\Omega}, \boldsymbol{\Omega}')$ is the scattering phase function. The illustration of each term of (1) can be found in our previous study [13]. In (2), the interpretation of the first and second terms on the right hand is similar with (1). The third and fourth terms on the right hand denote the contribution of the fluorescence from each excitation wavelength in the excitation ($\lambda_{ex,i}$, $i = 1,2,\ldots,N_{ex}$) and overlapped ($\lambda_{ol,j}$, $j = 1,2,\ldots,$k-1) region to the selected emission wavelength in the overlapped region ($\lambda_{ol,k}$), respectively. In each term, $\eta_{QE}(\lambda)$ and $\eta_{SS}(\lambda)$ represent the quantum efficiency and Stokes shift efficiency at each excitation wavelength, respectively. It should be noted that only a part of the converted light generated by each excitation wavelength ($\lambda_{ex,i}$ or $\lambda_{ol,j}$) will be emitted within the selected wavelength $\lambda_{ol,k}$. Hence, we introduce an emission weight $\omega(\lambda_{ex}, \lambda_{em})$ to describe the ratio of the converted light energy within the selected emission wavelength $\lambda_{em}$ to all the converted light energy generated by the excitation wavelength $\lambda_{ex}$, which can be expressed as:

$$\omega(\lambda_{ex},\lambda_{em}) = \begin{cases} 0, & 380 \le \lambda_{em} \le \lambda_{c,1} \\ \frac{f_{em}(\lambda_{em})}{\int_{\lambda_{c,1}}^{780} f_{em}(\lambda)d\lambda}, & 380 \le \lambda_{ex} \le \lambda_{c,1} \\ \frac{f_{em}(\lambda_{em})}{\int_{\lambda_{ex}}^{780} f_{em}(\lambda)d\lambda}, & \lambda_{c,1} < \lambda_{ex} \le \lambda_{c,2} \\ 0, & \lambda_{ex} > \lambda_{c,2} \end{cases} \quad (4)$$

It should be noted that the emission weight can be easily obtained from the emission spectrum $f_{em}$. Based on the definition of the emission weight, the Stokes shift efficiency $\eta_{SS}(\lambda)$ can be easily expressed as the ratio of the excitation wavelength to the weighted average of emission wavelength [17]:

$$\eta_{SS}(\lambda_{ex}) = \frac{\lambda_{ex}}{\int_{\max(\lambda_{ex},\lambda_{c,1})}^{780}\omega(\lambda_{ex},\lambda_{em})\cdot\lambda_{em}d\lambda_{em}} \quad (5)$$

It should be also noted that the emission weight is normalized so that the integration over the entire emission wavelength region is 1. The re-absorption effect can be easily included by using this weight in our model. The expression of (3) is very similar to (2) except that all the excitation wavelength in the overlapped region ($\lambda_{ol,j}$, $j = 1,2,\ldots,N_{ol}$) can contribute to the fluorescence.

After establishing the governing equations, the general boundary conditions are then presented. As shown in Fig. 1, boundary 1 (z = 0) denotes the incidence of the external blue LED light source with a typical Lambertian angular intensity distribution and a spectral flux distribution shown in Fig. 2. Boundary 2 (z = 0) is the diffuse reflection at the substrate or the reflector surface characterized by the diffuse reflectivity. And boundary 3 (z = d) is the Fresnel reflection at the phosphor-air interface due to the refractive index mismatch of the phosphor layer and the surrounding air. For each wavelength, these boundary conditions are applied. The details of the boundary conditions can be found in the previous work [13].

To calculate the spectral radiance $I(z, \boldsymbol{\Omega}, \lambda)$, the governing Eqs. (1)–(3) together with the boundary conditions are solved using SEM. First, the input parameters, appearing in the governing equations and boundary conditions, need to be obtained. Then, the wavelength, spatial and angular domains need to be discretized. The wavelength domain discretization has been illustrated above. The method for discretizing the spatial and angular domains is same with [13]. Next, the multi-wavelength FRTEs are solved from the shorter wavelength to the longer wavelength by step. For each wavelength, the solution procedure is similar to the previous method of solving two-wavelength FRTEs except for the calculation of emission weight. The spectral radiance is iteratively calculated by solving the corresponding discrete-ordinates equation. If the stop criterion, which means that the maximum relative error of the spectral radiance is below $10^{-4}$, is satisfied, the iteration process terminates. The spectral radiance in the excitation, overlapped and emission regions can be all obtained in sequence by using the same method.

Finally, the overall optical performance can be extracted from the spectral radiance $I(z, \boldsymbol{\Omega}, \lambda)$. The internal spectral radiant flux $S(z, \lambda)$ can be derived as the integration of $I(z, \boldsymbol{\Omega}, \lambda)$ over the total solid angle:

$$S(z,\lambda) = \int_{4\pi} I(z,\boldsymbol{\Omega},\lambda)d\Omega \quad (6)$$

Then, the radiant flux $\Phi(z)$ can be calculated as the integration of $S(z, \lambda)$ over the full wavelength region at each solution node:

$$\Phi(z) = \int_{380}^{780} S(z,\lambda)d\lambda \quad (7)$$

For a fluorescent material, the output optical properties are always important. Based on the definition of the Fresnel reflection of boundary 3, when the incident angle $\theta$ is below the critical angle $\theta_c$, the transmitted spectral radiant intensity $I_{out}(\theta_t, \varphi, \lambda)$ with a transmitted angle of $\theta_t$ at z = d can be expressed as:

$$I_{out}(\theta_t,\varphi,\lambda) = [1 - R(\cos\theta)]\cdot I(d,\theta,\varphi,\lambda), \quad \theta < \theta_c \quad (8)$$

where $R$ denotes the specular reflectivity and can be obtained referred to [13]. It can be seen that the obtained $I_{out}(\theta_t, \varphi, \lambda)$ contains both the angular and spectral distribution and can be used to calculate the angular CCT distribution according to [23]. Also, other output optical properties, including the spectral radiant flux, optical power, luminous flux, average CCT, and CRI (represented by Ra), can all be directly calculated using $I_{out}(\theta_t, \varphi, \lambda)$ [23].

In addition to the optical performance, the thermal performance can also be evaluated using this model. Considering the light-to-heat process, the heat generation density versus invasion depth $q(z)$ can be calculated as the sum of the unconverted part of the absorbed spectral radiant flux at each wavelength:

$$q(z) = \int_{380}^{780}\left[\kappa_a(\lambda_{ex}) - \kappa_a(\lambda_{ex})\cdot\eta_{QE}(\lambda_{ex})\cdot\int_{\lambda_{ex}}^{780}\eta_{SS}(\lambda_{ex})\omega(\lambda_{ex},\lambda_{em})d\lambda_{em}\right] \cdot S(z,\lambda_{ex})d\lambda_{ex} \quad (9)$$

By inputting the $q(z)$ as a distributed heat source into the heat diffusion equation, we can further obtain the temperature distribution within the phosphor layer [24–27]. In this process, the optical parameters are assumed to be independent on temperature.

## 3. Experiments

To verify the multi-wavelength model, a remote pc-LED module same with [13] was fabricated. A commercial YAG: Ce yellow phosphor (YAG-04, Intematix Inc.) was used in our experiment. To prepare the phosphor film, the phosphor powder was mixed with the transparent silicone matrix (Dow Corning OE-6550 A and B in 1:1 mix ratio) with

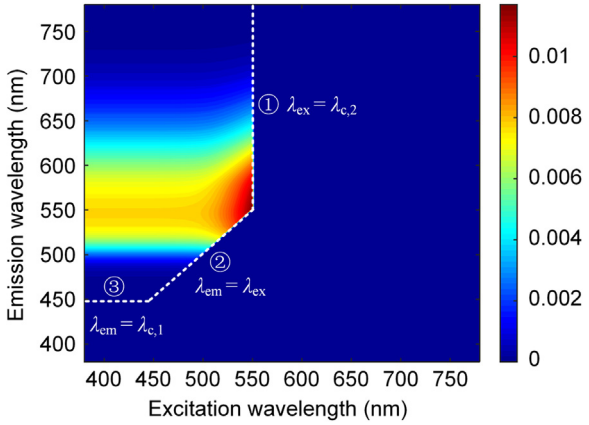


**Fig. 3.** The emission factor calculated from the emission spectrum in Fig. 2 using (4).

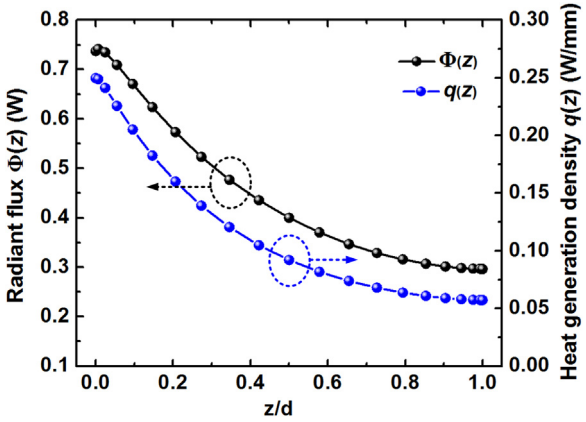


**Fig. 4.** The radiant flux Φ(z) and heat generation density $q$(z) versus normalized invasion depth z/d.

varying phosphor concentration from 0.05 g/cm$^3$ to 0.30 g/cm$^3$ with an interval of 0.05 g/cm$^3$. A commercial LED module bonded with a substrate was assembled with a designed reflector with a reflectivity of 0.8. Then the phosphor film was directly placed onto the reflector. The optical performances of the pc-LED module, including the spectrum, optical power, luminous flux, average CCT, and CRI, under driving current of 0.35 A and different phosphor concentrations were measured using an integrating sphere (ATA-1000, Everfine Inc.). In addition, the angular CCT and spectral radiant intensity distribution were measured using the same experimental setup with [13].

## 4. Results and discussions

To implement the model, some input parameters need to be obtained at first. The excitation, emission spectrum and the quantum efficiency of the used YAG: Ce phosphor were adopted from the experimental data published in [28], as shown in Fig. 2. We can see that a large spectral overlap occurs between 450 nm and 550 nm. The excitation region ranges from 380 nm to 450 nm and the emission wavelength ranges from 550 nm to 780 nm. Fig. 3 shows the emission weight calculated from the emission spectrum using (4). We can see that there are three critical lines dividing the figure into two parts. The emission weight is greater than zero on the condition that the excitation wavelength is lower than $\lambda_{c,2}$ (550 nm), the emission wavelength is higher than the excitation wavelength, and the emission wavelength is higher than $\lambda_{c,1}$ (450 nm). The maximum weight is located at the peak emission wavelength. By inputting the wavelength-dependent absorption coefficient of the YAG: Ce crystal phosphor adopted from [29], we calculated the wavelength-dependent absorption and scattering coefficients of the phosphor/silicone mixture using Mie theory [30]. In this work, we use the Henyey-Greenstein (HG) phase function and the anisotropy parameter is calculated to be 0.82 [13]. The refractive index of the phosphor plate is set to be 1.53 [1]. The LED emission spectrum is also plotted in Fig. 2 with a peak wavelength of 450 nm and the total output optical power is measured to be 0.41 W under 0.35 A. The following results are all based on these conditions. The multi-wavelength model is implemented by coding in the commercial software Matlab using a 3.3-GHz Intel(R) Core(TM) i3–3220 processor. The computing time is only 5.2 min even when the total discrete number reaches $6.56 \times 10^5$. And the computing time can be reduced significantly by using an advanced processer. When it comes to the Monto-Carlo simulation, the total computing time can be usually over hours or even more. Hence, the presented analytical method is more computational efficient than the Monto-Carlo simulation.

Fig. 4 plots the radiant flux Φ(z) and heat generation density $q$(z) versus normalized invasion depth z/d calculated by (7) and (9), respectively. We can see that the radiant flux decreases with invasion depth because the light absorption dominates the light propagation process. The heat generation density exhibits a similar trend with the radiant flux due to the fact that the heat is generated from the absorbed radiant flux.

Fig. 5 shows the comparisons of the output spectral radiant flux distribution between the experiment and model prediction under phosphor concentration of 0.05 g/cm$^3$, 0.15 g/cm$^3$, and 0.30 g/cm$^3$, respectively. We can see that the spectrum has two peaks, corresponding to the LED peak wavelength (450 nm) and phosphor peak emission wavelength (540 nm). It can be easily understood that as the concentration increases, the flux of the blue peak decreases rapidly and that of the yellow peak rises. For three concentrations, the calculated spectrum matches well with the measurement in terms of the overall trend and shape. The deviation mainly occurs at the two peaks. It is because that the input parameters, including the absorption, scattering coefficients, and the phase function, do not match very well with the actual case and the effect is enlarged at the peaks. Even so, the maximum deviation is 7.6%, demonstrating the accuracy of the presented model.

Using the spectrum presented in Fig. 5, we also calculated the overall optical performances including optical power, luminous flux, average CCT, and CRI (Ra). Fig. 6 shows the comparison of these properties between the measurement and calculation. We can see that the optical power rises constantly with concentration due to the increased light absorption. The luminous flux rises instead with concentration because the optical power in the green-yellow range increases and this part contributes more to the luminous flux [23]. As the concentration rises, both the average CCT and CRI decrease. For the four properties, overall good agreements are achieved with similar developing trends and relative close values. And the maximum deviation among those properties is 4.1%, which is occurred at 0.05 g/cm$^3$ for the luminous flux.

In addition, the angular optical performance is also calculated and compared. Fig. 7(a) plots the measured and calculated angular CCT distribution. In low view angle, the calculated CCT agrees well with the measured CCT. There exists deviation when the view angle increases with the maximum deviation of 3.6%. The main source of the deviation may lie in the estimates of the input parameters and the smooth surface assumption. We further compare the measured and calculated normalized spectral radiant intensity at different angles. Fig. 7(b) to (d) show the comparisons of three representative view angles of 1.4°, 30.2°, and 58.3° with corresponding simulated CCT of 7658 K, 6868 K, and 5848 K, respectively. The values of these view angles are determined by the angular discretization and Fresnel boundary condition. As the view angle rises, the relative power in yellow region increases, corresponding to a decrease in CCT. For three angles, the spectral radiant intensity obtained by the experiment and model shows good agreement

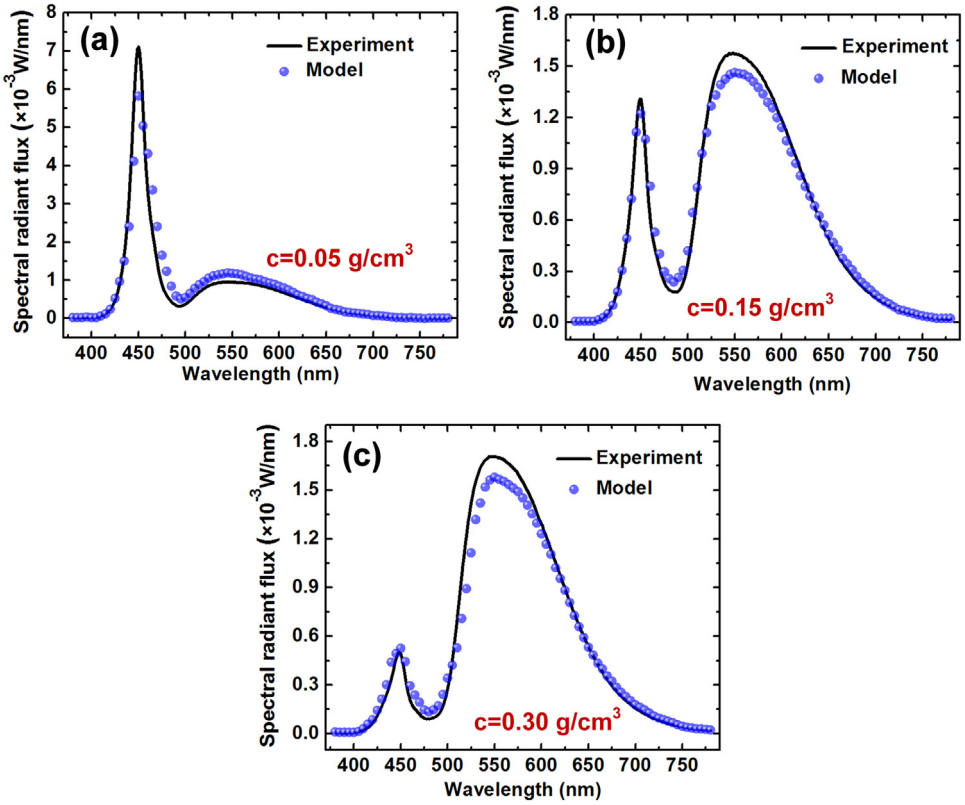


**Fig. 5.** Comparisons of the output spectral radiant flux distribution between the experiment and model at different phosphor concentration of (a) 0.05 g/cm$^3$, (b) 0.15 g/cm$^3$, and (c) 0.30 g/cm$^3$, respectively.

with similar trend and close values. As a whole, the presented model is accurate enough to model the light propagation properties and evaluate the spectral and angular performance of phosphor material.

Finally, we compare the previous two-wavelength model and the presented multi-wavelength model. Fig. 8 plots the total optical power $P_{out}$, blue light power $P_{out,B}$, and yellow light power $P_{out,Y}$ calculated by these two models. For the convenience of comparison, $P_{out,B}$ and $P_{out,Y}$ are defined as the integration of the spectral flux over the wavelength of

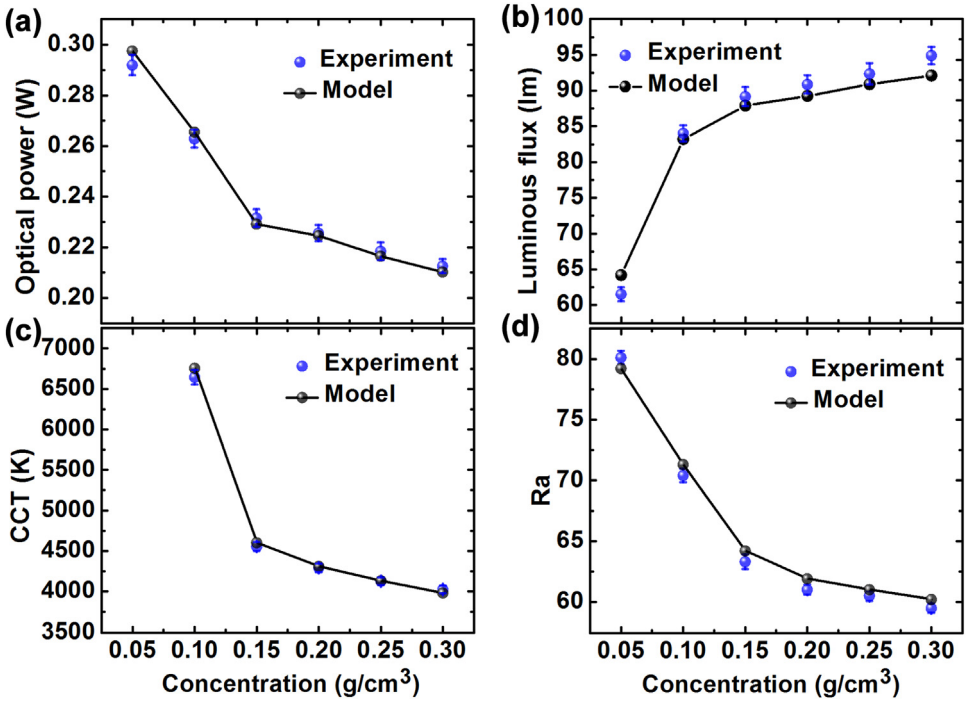


**Fig. 6.** Comparisons of optical performance: (a) optical power, (b) luminous flux, (c) average CCT, and (d) color rendering index (Ra) between experiment and model versus varying phosphor concentration from 0.05 g/cm$^3$ to 0.30 g/cm$^3$ with an interval of 0.05 g/cm$^3$.

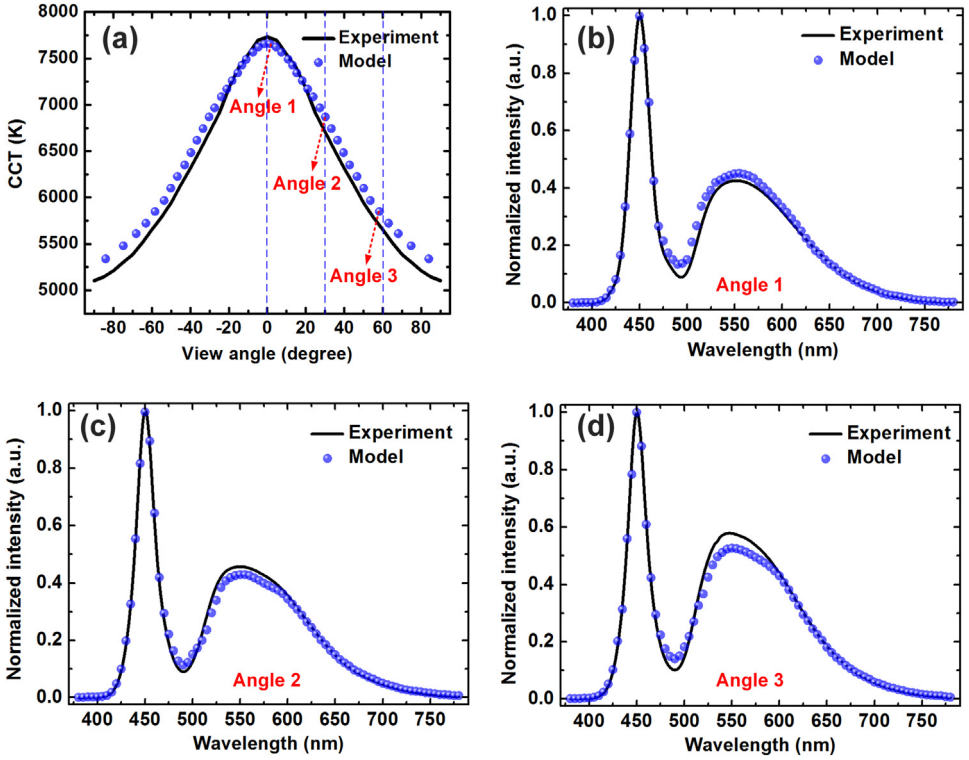


**Fig. 7.** Comparisons of the (a) angular CCT distribution, and normalized spectral radiant intensity at varying angles of (b) 1.4°, (c) 30.2°, and (d) 58.9° between experiment and model at phosphor concentration of 0.10 g/cm$^3$.

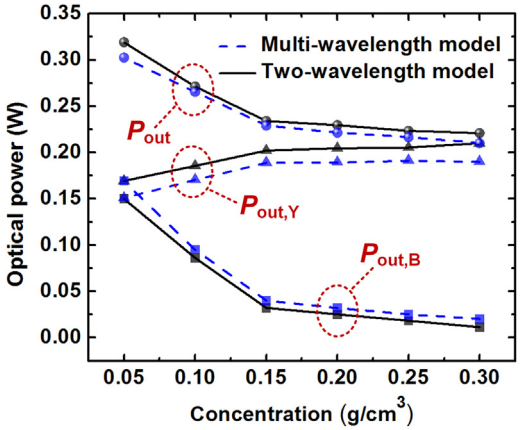


**Fig. 8.** Comparisons of the optical power of whole wavelength region $P_{out}$, blue light region $P_{out,B}$, and yellow light region $P_{out,Y}$ between two-wavelength model and multi-wavelength model with varying phosphor concentration.

blue light range and yellow light range, respectively. According to [30], light with spectra from 380 nm to 490 nm is defined as blue light, and light with spectra from 490 nm to 780 nm is defined as yellow light. We can see that $P_{out,B}$ obtained by the two-wavelength model is lower than that by the multi-wavelength model, whereas the case of $P_{out,Y}$ is just in the opposite. It is due to that for all the excitation wavelengths, the absorption coefficient and quantum efficiency are both assumed to be identical to the peak absorption coefficient and the peak quantum efficiency at peak excitation wavelength in the two-wavelength model. In this case, more blue light will be absorbed and more yellow light will be converted, which may further cause deviation in predicting the chromatic properties. As for the total optical power, it is interesting to see that $P_{out}$ calculated by these two models matches with each other, indicating that both two models are feasible in predicting $P_{out}$. This is also consistent with our previous literature [13].

## 5. Conclusions

In this work, we presented an extended multi-wavelength model based on the fluorescent radiative transfer equation to describe the simultaneous light absorption, scattering, fluorescence, and re-absorption processes. The re-absorption effect was included by introducing an emission weight in this model. The spectral radiance at any spatial location and angular direction for each wavelength was calculated by solving the multi-wavelength FRTEs using SEM. The presented model was validated by comparing the predicted spectrum and angular CCT with the experiments, with the corresponding maximum deviation of 7.6% and 3.6%, respectively. We also compared the two-wavelength model with the presented model and found that the two-wavelength model may underestimate or overestimate the optical power in the blue and yellow region, respectively. Moreover, the presented model can be easily coupled into the heat diffusion equation to evaluate the thermal and further the optical-thermal interacted performances. In summary, the efficient and accurate multi-wavelength model can be very useful in predicting the angular, spectral and even thermal properties of phosphor and other fluorescent media.

## Acknowledgements

This work was supported by the National Natural Science Foundation of China (51625601, 51576078, and 51606074), in part by the National Key Research and Development Program of China (2016YFB0100901 and 2016YFB0400804), and in part by the Ministry of Science and Technology of the People's Republic of China (2017YFE0100600).

## References

[1] X.B. Luo, R. Hu, S. Liu, K. Wang, Heat and fluid flow in high-power LED packaging and applications, Prog. Energy Combust. Sci. 56 (2016) 1–32.
[2] Y.P. Ma, W. Lan, B. Xie, R. Hu, X.B. Luo, An optical-thermal model for laser-excited

remote phosphor with thermal quenching, Int. J. Heat. Mass Transf. 116 (2018) 694–702.
[3] A. Lenef, J.F. Kelso, A. Piquette, Light extraction from luminescent light sources and application to monolithic ceramic phosphors, Opt. Lett. 39 (10) (2014) 3058–3061.
[4] Y.P. Ma, R. Hu, X.J. Yu, W.C. Shu, X.B. Luo, A modified bidirectional thermal resistance model for junction and phosphor temperature estimation in phosphor-converted light-emitting diodes, Int. J. Heat. Mass Transf. 106 (2017) 1–6.
[5] C.C. Sun, Y.Y. Chang, Y.H. Wang, C.Y. Chen, Y.C. Lo, H.H. Cheng, Precise spatial-color optical modeling in phosphor-converted white LEDs, J. Disp. Technol. 11 (3) (2015) 261–265.
[6] C. Sommer, J.R. Krenn, P. Hartmann, P. Pachler, M. Schweighart, S. Tasch, F.P. Wenzl, The effect of the phosphor particle sizes on the angular homogeneity of phosphor-converted high-power white LED light sources, IEEE J. Sel. Top. Quant. 15 (4) (2009) 1181–1188.
[7] R. Hu, X.B. Luo, H. Zheng, Hotspot location shift in the high power phosphor converted white light-emitting diode package, Jpn. J. Appl. Phys. 51 (9S2) (2012) (Art. no. 09MK05).
[8] J. Chen, X. Intes, Comparison of Monte Carlo methods for fluorescence molecular tomography computational efficiency, Med. Phys. 38 (10) (2011) 5788–5798.
[9] A. Lenef, J. Kelso, M. Tchoul, O. Mehl, J. Sorg, Y. Zheng, Laser-activated remote phosphor conversion with ceramic phosphors, in: Proceedings of the SPIE 9190, San Diego, CA, USA, 2014, pp. 919000C.
[10] T. Shakespeare, J. Shakespeare, A fluorescent extension to the Kubelka–Munk model, Color Res. Appl. 28 (1) (2003) 4–14.
[11] D.Y. Kang, E. Wu, D.M. Wang, Modeling white light-emitting diodes with phosphor layers, Appl. Phys. Lett. 89 (23) (2006) (Art. no. 231102).
[12] R. Hu, X.B. Luo, H. Feng, S. Liu, Effect of phosphor settling on the optical performance of phosphor converted LED, J. Lumin 132 (2012) 1252–1256.
[13] Y.P. Ma, M. Wang, J. Sun, R. Hu, X.B. Luo, Phosphor modeling based on fluorescent radiative transfer equation, Opt. Express 26 (13) (2018) 16442–16455.
[14] C.H. Hung, C.H. Tien, Phosphor-converted LED modeling by bidirectional photometric data, Opt. Express 18 (S3) (2010) A261–A271.
[15] C.C. Sun, C.Y. Chen, H.Y. He, C.C. Chen, W.T. Chien, T.X. Lee, T.H. Yang, Precise optical modeling for silicate-based white LEDs, Opt. Express 16 (24) (2008) 20060–20066.
[16] S.W. Jeon, J.H. Noh, K.H. Kim, W.H. Kim, C.H. Yun, S.B. Song, J.P. Kim, Improvement of phosphor modeling based on the absorption of Stokes shifted light by a phosphor, Opt. Express 22 (S5) (2014) A1237–A1242.
[17] S. Leyre, G. Durinck, B.V. Giel, W. Saeys, J. Hofkens, G. Deconinck, P. Hanselaer, Extended adding-doubling method for fluorescent applications, Opt. Express 20 (16) (2012) 17856–17872.
[18] K. Sakuma, N. Hirosaki, R.J. Xie, Red-shift of emission wavelength caused by reabsorption mechanism of europium activated Ca-α-SiAlON ceramic phosphors, J. Lumin. 126 (2) (2007) 843–852.
[19] S. Leyre, M. Withouck, G. Durinck G, J. Hofkens, G. Deconinck, P. Hanselaer, Modelling fluorescent materials with a spectral overlap between excitation and emission spectrum, in: Proceedings of the 2nd International Conference on Photonics, Optics and Laser Technology, Portugal, 2014, pp. 33–38.
[20] A.T. Patera, A spectral element method for fluid dynamics-laminar flow in a channel expansion, J. Comput. Phys. 54 (1984) 468–488.
[21] J.M. Zhao, L.H. Liu, Least-squares spectral element method for radiative heat transfer in semitransparent media, Numer. Heat. Transf. B 50 (5) (2006) 473–489.
[22] A.D. Klose, Radiative transfer of luminescence light in biological tissue, Light Scattering Reviews, Springer, 2009, p. 4.
[23] E.F. Schubert, Light-emitting Diodes, Cambridge Univ. Press, 2003.
[24] J.M. Zhao, L.H. Liu, Spectral element approach for coupled radiative and conductive heat transfer in semitransparent medium, J. Heat. Transf. 129 (10) (2007) 1417–1424.
[25] B.F. Shang, Y.P. Ma, R. Hu, C. Yuan, J.Y. Hu, X.B. Luo, Passive thermal management system for downhole electronics in harsh thermal environments, Appl. Therm. Eng. 118 (2017) 593–599.
[26] R. Hu, S.L. Zhou, Y. Li, D.Y. Lei, X.B. Luo, C.W. Qiu, Illusion thermotics, Adv. Mater. 30 (2018) 1707237.
[27] S.L. Zhou, R. Hu, X.B. Luo, Thermal illusion with twinborn-like heat signatures, Int. J. Heat. Mass Transf. 127 (2018) 607–613.
[28] K. Du, H.K. Li, K.Q. Guo, H. Wang, D.C. Li, W.D. Zhang, T. Mei, S.J. Chua, The rate equation based optical model for phosphor-converted white light-emitting diodes, J. Phys. D: Appl. Phys. 50 (9) (2017) (Art. no. 095101).
[29] M. Kučera, P. Hasa, J. Hakenová, Optical and magneto-optical properties of Ce:YAG, J. Alloy. Compd. 451 (1–2) (2008) 146–148.
[30] Z.Y. Liu, S. Liu, K. Wang, X.B. Luo, Measurement and numerical studies of optical properties of YAG: Ce phosphor for white LED packaging, Appl. Opt. 49 (2) (2010) 247–257.